Incorporation of a wave-packet propagation method into the *S*-matrix framework: Investigation of the effects of excited state dynamics on intense-field ionization

Manabu Kanno, Tsuyoshi Kato, Hirohiko Kono,* and Yuichi Fujimura
Department of Chemistry, Graduate School of Science, Tohoku University, Sendai 980-8578, Japan

Farhad H. M. Faisal
Fakultät für Physik, Universität Bielefeld, Postfach 100131, D-33501 Bielefeld, Germany
(Received 19 May 2005; revised manuscript received 1 August 2005; published 28 September 2005)

We propose a theoretical method for investigation of ionization of atoms and molecules in intense laser fields that copes with the effects of excited state dynamics (or intramolecular electronic dynamics). The time-evolving wave packet composed of only bound electronic states, $|\Phi_i(t)\rangle$, is introduced into a framework of the intense-field *S*-matrix theory. Then, the effects of both Coulomb field and radiation field on the bound electron(s) are well described by $|\Phi_i(t)\rangle$, while the effects of a radiation field on a freed electron are also treated in a nonperturbative way. We have applied the theory to ionization of H and H_2^+ in ultrashort intense laser pulses. Although only a small number of Gaussian functions are used in the expansion of $|\Phi_i(t)\rangle$, the present method can quantitatively reproduce the features of enhanced ionization of H_2^+ obtained by an accurate grid propagation method. This agreement supports the view that field-induced population transfer between the lowest two electronic states triggers the enhancement of ionization at large internuclear distances. We also applied the method to calculate the photoelectron momentum distribution of H in an intense near-infrared field. A broad low intensity component due to "rescattering" appears in the distribution of the momentum perpendicular to the polarization direction of an applied laser field, as observed in the experiments of single ionization of noble gas atoms. The present method provides a practical way of properly describing the nonperturbative nature of field-induced dynamics of an electron (or electrons) in the presence of both Coulomb and radiation fields.

DOI: 10.1103/PhysRevA.72.033418 PACS number(s): 32.80.Rm, 33.80.Rv, 34.50.Gb, 42.50.Hz

I. INTRODUCTION

Originally the *S*-matrix theory for obtaining the transition probability of a quantum process was introduced by Heisenberg in 1943 [1] for stationary systems in general, and since has been extensively used for a wide range of problems in high-energy physics, nuclear physics, and atomic and molecular scattering. Generally an element of the *S* matrix is equivalent to the transition amplitude obtained by the standard prescription of projection of the final state onto the total wave funtion of the system, evaluated in the long-time limits. Since the early days of nonperturbative ionization of atoms in intense laser fields several versions have been introduced which are together known as the Keldysh-Faisal-Reiss (KFR) theory [2–4]. More recently this theory has been extended to many-body problems in intense laser fields [5,6], which is called the intense-field many-body *S*-matrix theory (IM*S*T). It has been applied to ionization of multielectron atoms and molecules in intense laser fields [7]. In these applications, only the leading terms of systematic series expansions for ionization processes have been used.

On the other hand, direct quantum mechanical simulations of ionization dynamics have been carried out by accurately solving the time-dependent Schrödinger equation (TDSE); e.g., accurate propagation of an electronic wave functions of one- and two-electron molecules H_2^+ and H_2 can be performed by using the dual transformation method[8–11]. In the method, both wave function and the Hamiltonian are consistently transformed to special forms so that the numerical difficulties arising from the divergence of the Coulomb potentials are overcome . In most cases of the direct numerical approaches, the time-dependent wave function is represented in terms of the amplitudes at a number of grid points. One can estimate the ionization probabilities of H_2^+ and H_2 in intense near-infrared fields by setting absorbing boundaries at the ends of a large grid space. The dependence of the calculated ionization probabilities of H_2^+ and H_2 on the internuclear distance is in accordance with the experimentally observed tendency that ionization of a molecule in a near-infrared laser field is greatly enhanced at critical internuclear distances which are much larger than the equilibrium internuclear distance (known as enhanced ionization) [12]. The analysis of the entire electronic wave packet indicates that acceleration or suppression of field-induced intramolecular electron transfer leads to enhanced ionization [8–11]. An electron or electrons move inside a molecule before ionization takes place.

Enhanced ionization, which leads to Coulomb explosions, is a universal phenomenon irrespective of whether the molecule is diatomic [13] or polyatomic [14]. It is shown that field-induced intramolecular electronic dynamics also causes chemical reaction (fragmentation) dynamics of diatomic or polyatomic molecules [11,15]. Intramolecular electronic dynamics, which triggers both enhanced ionization and reaction dynamics, is therefore regarded as the key process to control

*Electronic address: kono@mcl.chem.tohoku.ac.jp

the competition between ionization and reaction of molecules [16]. To investigate the competing processes of molecules in intense laser fields, one must calculate the ionization probability as a function of the positions of nuclei. To that end, introduction of bound excited states associated with intramolecular electronic dynamics into a theoretical framework is inevitable. Although a thorough description of bound state dynamics is obtained by accurate wave-packet propagation based on grid point representations, it is however impossible to strictly apply the grid point method to a general multielectron system because a quantum representation of the system requires an enormous number of grid points.

In this paper, we propose a feasible way of including effects of bound state dynamics in a theoretical treatment. This can be achieved by taking advantage of the strong points of both the *S*-matrix theory and the wave-packet approach. As clearly demonstrated by the IM*S*T, the usual *S*-matrix series expansion of the transition amplitude of a process can be rearranged in a systematic way that the chosen leading terms are essential for the description of the process. On the other hand, the wave-packet approach is intended for nonperturbative treatment of interactions because wave-packet propagation is usually performed by directly solving appropriate equations of motion. The central idea we propose is to introduce a time-dependent wave function $|\Phi_i(t)\rangle$ expanded in terms of bound electronic states only. We then incorporate this key wave packet $|\Phi_i(t)\rangle$ into the framework of the intense-field *S*-matrix theory to calculate the amplitudes of transition to ionization continuum states. Accurate propagation of $|\Phi_i(t)\rangle$ in the presence of an alternating electric field can be executed by numerically solving a set of coupled differential equations for expansion coefficients. Since the Hilbert space for expansion is restricted to a space of bound states, basis set expansion techniques elaborated in the field of quantum chemistry can be utilized to efficiently expand the molecular orbitals (MOs) or the wave functions of bound states in terms of a small number of Gaussian basis functions [17]. Thus, systematic account of electron correlation is also possible. MO representations or Gaussian basis sets are widely used in the KFR theory as well as in tunneling theory [18], but the wave functions treated in the theoretical formulations were essentially time independent. Our method is applicable to cases of ionization by ultrashort laser pulses.

To investigate the ability of our approach, we first apply it to one-electron systems of H_2^+ and H interacting with an intense ultrashort pulse. For one-electron systems, reference results are available. The ionization probability of H_2^+ calculated by the proposed approach as a function of the internuclear distance *R* successfully captures the main feature of enhanced ionization of H_2^+. To investigate the origin of this agreement, we analyze the time-dependent populations of bound states in $|\Phi_i(t)\rangle$ and in the entire wave packet $|\Psi_i(t)\rangle$. We also calculate photoelectron momentum distributions for ionization of H by an intense near-infrared pulse. The features of photoelectron momentum distributions calculated for H are discussed in connection with the distributions experimentally measured for single ionization of noble gas atoms and H_2 [19]. We demonstrate how the present method describes the nonperturbative nature of electronic dynamics in the presence of both Coulomb and laser fields.

II. THEORY

In this section, we present a way of combining the intense-field *S*-matrix theory and an electronic wave-packet approach that can describe bound excited state dynamics such as intramolecular electronic dynamics. We assume a general time-dependent Hamiltonian $\hat{H}(t)$ of the total system and partition it in two different ways:

$$\hat{H}(t) = \hat{H}_i(t) + \hat{H}_i'(t) = \hat{H}_f(t) + \hat{H}_f'(t), \tag{1}$$

where $\hat{H}_i(t)$ is the reference Hamiltonian for an initial state, $\hat{H}_f(t)$ is the reference Hamiltonian for a chosen "final" state, and $\hat{H}_i'(t)$ and $\hat{H}_f'(t)$ are the respective interaction Hamiltonians. $|\psi_i(t)\rangle$ and $|\phi_f(t)\rangle$ are assumed to be the known solutions of the corresponding TDSEs for $\hat{H}_i(t)$ and $\hat{H}_f(t)$. The TDSE of the total system is

$$i\frac{\partial}{\partial t}|\Psi_i(t)\rangle = \hat{H}(t)|\Psi_i(t)\rangle, \tag{2}$$

where the initial condition is $|\Psi_i(t_0)\rangle = |\psi_i(t_0)\rangle$. Atomic units are used in this paper unless otherwise noted.

There are various formal expressions for the solution of Eq. (2). In this study, we employ the "post" form for $|\Psi_i(t)\rangle$, which can be written down formally as [6,20,21]

$$|\Psi_i(t)\rangle = \hat{U}_f(t,t_0)|\psi_i(t_0)\rangle - i\int_{t_0}^{t} d\tau \hat{U}_f(t,\tau)\hat{H}_f'(\tau)|\Psi_i(\tau)\rangle, \tag{3}$$

where $\hat{U}_f(t,t_0)$ is the time-evolution operator for $\hat{H}_f(t)$, and it satisfies the following equation:

$$i\frac{\partial}{\partial t}\hat{U}_f(t,t_0) = \hat{H}_f(t)\hat{U}_f(t,t_0) \tag{4}$$

with the condition $\hat{U}_f(t_0,t_0)=1$. Equation (3) evaluated at $t=t_0$ obviously satisfies the initial condition $|\Psi_i(t_0)\rangle = |\psi_i(t_0)\rangle$. Using Eq. (4), one can easily verify that Eq. (3) fulfills Eq. (2).

The system of our interest is an atom or a molecule interacting with a classical laser field. Now $\hat{H}_i(t)$ is the Hamiltonian for the system without a laser field and $\hat{H}_i'(t)$ is the radiative interaction between the system and the laser field. Our choice of $\hat{H}_f(t)$ and $\hat{H}_f'(t)$ is as follows: $\hat{H}_f(t)$ is the sum of the Hamiltonian for a free electron in the laser field and that for the remaining ion in the laser field; $\hat{H}_f'(t)$ is the binding potential exerted on the freed electron by the remaining ion. The transition amplitude to the true final continuum state $|\psi_f(t)\rangle$ for the field-free Hamiltonian $\hat{H}_i(t)$ is obtained by projecting $\langle\psi_f(t)|$ from the left onto the exact time-evolving wave packet $|\Psi_i(t)\rangle$. Since the final state of our interest is one of continuum states, only the continuum state

component of $|\Psi_i(t)\rangle$ contributes to the projection. Thus, in this case, the desired S-matrix element for the transition from $|\psi_i(t_0)\rangle$ to $|\psi_f(t=\infty)\rangle$, $S_{fi} \equiv \lim_{t\to\infty}\langle\psi_f(t)|\Psi_i(t)\rangle$, can be formally expressed as

$$S_{fi} = \lim_{t\to\infty}\langle\psi_f(t)|\left[|\Psi_i(t)\rangle - \sum_b |\psi_b(t)\rangle\langle\psi_b(t)|\Psi_i(t)\rangle\right], \quad (5)$$

where the summation is taken over bound states $\{|\psi_b(t)\rangle\}$ to extract the continuum states from $|\Psi_i(t)\rangle$ ($\{|\psi_b(t_0)\rangle\}$ are bound states of $\hat{H}_i(t_0)$). Note that $\langle\psi_f(t)|\psi_b(t)\rangle = 0$. Inserting Eq. (3) into Eq. (5) gives the exact element of the S matrix. As will be shown later, we start with the formal expression of Eq. (5) to estimate the transition amplitudes to final continuum states.

Here, we introduce the wave packet composed of bound states only, $|\Phi_i(t)\rangle$:

$$|\Phi_i(t)\rangle = \sum_b c_{ib}(t)|\psi_b(t)\rangle, \quad (6)$$

where $c_{ib}(t)$ are expansion coefficients and the initial condition is given by $|\Phi_i(t_0)\rangle = |\psi_i(t_0)\rangle$. By inserting $|\Phi_i(t)\rangle$ into the TDSE for the total Hamiltonan, we then obtain the following coupled equations of motion for the determination of $c_{ib}(t)$:

$$i\frac{d}{dt}c_{ib}(t) = \sum_{b'} c_{ib'}(t)\langle\psi_b(t)|\hat{H}_i'(t)|\psi_{b'}(t)\rangle. \quad (7)$$

The obtained wave packet $|\Phi_i(t)\rangle$ for bound state dynamics can be used to make a practical evaluation of Eq. (5) as follows.

(i) First, we replace the bound state component $\Sigma_b|\psi_b(t)\rangle\langle\psi_b(t)|\Psi_i(t)\rangle$ in Eq. (5) with $|\Phi_i(t)\rangle$. A quantitative comparison between $\Sigma_b|\psi_b(t)\rangle\langle\psi_b(t)|\Psi_i(t)\rangle$ and $|\Phi_i(t)\rangle$ will be made later.

(ii) Second, $|\Psi_i(\tau)\rangle$ in the integral in the right-hand side of Eq. (3) is replaced by $|\Phi_i(\tau)\rangle$. This replacement is justified by the consideration that the dominant contribution to the integral comes from the bound state component of $|\Psi_i(\tau)\rangle$. The resultant approximate wave function for $|\Psi_i(t)\rangle$ is denoted by $|\tilde{\Psi}_i(t)\rangle$. We replace the first term in the square brackets of Eq. (5), $|\Psi_i(t)\rangle$, by $|\tilde{\Psi}_i(t)\rangle$. The continuum state component in Eq. (5) is thus approximated by $|\tilde{\Psi}_i(t)\rangle - |\Phi_i(t)\rangle$.

In the first version of the present theoretical treatment, a further simplification is made; we use the strong-field approximation in which the final continuum state $|\psi_f(t)\rangle$ is substituted by $|\phi_f(t)\rangle$, i.e., the product of a one-electron Volkov state and a state of the remaining ion. The physical meaning of the substitution $|\psi_f(t)\rangle \to |\phi_f(t)\rangle$ is that a photoelectron no longer feels the binding potential after transferred to a continuum state.

Taking the above two steps (i) and (ii) together with the introduction of the strong-field approximation, we can replace Eq. (5) by a formula to estimate the S-matrix elements properly:

$$S_{fi} \simeq \lim_{t\to\infty}\langle\phi_f(t)|\left[|\tilde{\Psi}_i(t)\rangle - |\Phi_i(t)\rangle\right] = \lim_{t_0\to-\infty,t\to\infty}\left[\langle\phi_f(t_0)|\psi_i(t_0)\rangle - i\int_{t_0}^{t} d\tau\langle\phi_f(\tau)|\hat{H}_f'(\tau)|\Phi_i(\tau)\rangle - \langle\phi_f(t)|\Phi_i(t)\rangle\right]. \quad (8)$$

The Volkov state $|\phi_f(t)\rangle$ has nonzero overlaps with the bound states in $|\Psi_i(t)\rangle$ or $|\tilde{\Psi}_i(t)\rangle$. This defect of the Volkov state can be redeemed by subtracting bound states from the total wave function at $t=\infty$ (or when the applied field is turned off), as in Eq. (8). Equation (8) certainly satisfies the requirement that S_{fi} must be zero when $\hat{H}_i'(t)=0$ for all t. Needless to say, the last term in Eq. (8) vanishes if $|\phi_f(t)\rangle$ is replaced by a true final continuum state $|\psi_f(t)\rangle$. Since $|\Phi_i(t)\rangle$ consists of many bound states, it can reproduce the field-induced mixing of bound excited states as in the dynamics of the exact wave packet $|\Psi_i(t)\rangle$. Therefore, Eq. (8) explicitly includes the effects of field-induced intramolecular electronic dynamics on ionization.

By using Eq. (8), we obtain the populations $\{|S_{fi}|^2\}$ of final continuum states $\{f\}$ in $|\tilde{\Psi}_i(t)\rangle - |\Phi_i(t)\rangle$. The total ionization probability is given by

$$W = \frac{V}{(2\pi)^3}\int d\mathbf{p}_f|S_{fi}|^2, \quad (9)$$

where the integration is done over all final states $\{f\}$ labeled as canonical momenta $\{\mathbf{p}_f\}$ of an electron freed from the ion core, V is a configuration space volume for normalization of the final states, and $(2\pi)^3$ is the size of a unit volume in phase space.

We finally specify the radiative interaction $\hat{H}_i'(t)$. First of all, the use of the dipole approximation is justified because we are mainly interested in the interaction with near-infrared light fields. Equation (8) does not formally restrict the options of the gauge of the field, yet gauge invariance is generally not preserved in numerical calculations using incomplete basis sets [22]. The explicit forms of $\hat{H}_i'(t)$ in the Coulomb and velocity gauges are $\mathbf{A}(t)\cdot(-i\nabla) + A^2(t)/2$ and $\mathbf{A}(t)\cdot(-i\nabla)$, respectively, where $\mathbf{A}(t)$ is the vector potential of the laser field; it is $\mathbf{r}\cdot\boldsymbol{\varepsilon}(t)$ in the length gauge, where $\boldsymbol{\varepsilon}(t)$ is the laser electric field. In this study, the length gauge was chosen to facilitate comparison of our results with those obtained from the accurate grid point method [8], in which the length gauge was also used. The results for different gauges will be reported elsewhere. The analytical form of the one-electron Volkov state $|\phi_f(t)\rangle$ of canonical momentum $\mathbf{p}_f$ in the length gauge is given by

$$|\phi_f(t)\rangle = \frac{1}{V^{1/2}}\exp\left\{-\frac{i}{2}\int_{t_0}^{t} d\tau[\mathbf{p}_f + \mathbf{A}(\tau)]^2\right\}|\mathbf{p}_f + \mathbf{A}(t)\rangle, \quad (10)$$

where

$$\langle\mathbf{r}|\mathbf{p}_f + \mathbf{A}(t)\rangle = \exp\{i[\mathbf{p}_f + \mathbf{A}(t)]\cdot\mathbf{r}\}. \quad (11)$$

In this study, following the idea of the conventional quantum chemistry, we expand the states used in $|\Phi_i(t)\rangle$ in terms of Gaussian basis functions. Then, it is routine to evaluate the matrix elements of $\hat{H}_i'(t)$ on the right-hand side of Eq. (7) [23]; the coupled equations in Eq. (7) can be solved by using conventional algorithms such as the Runge-Kutta method. In the case of one-electron systems, the matrix elements of the binding potential $\hat{H}_f'(t)$ between $|\phi_f(t)\rangle$ and $|\Phi_i(t)\rangle$ in Eq. (8), as well as the overlaps between them, are reduced to those between a plane wave (PW) and a Gaussian function (GF). A scheme for fast evaluation of the matrix elements is given in the Appendix. Integration with respect to τ in Eq. (8) is carried out numerically by the trapezoidal or Simpson's rule.

III. RESULTS AND DISCUSSION

In this section, we present the results of application of the present approach to one-electron systems. We calculated the ionization probabilities or photoelectron spectra of H and H_2^+ in intense laser fields. In the following results, the applied laser pulse is assumed to be a linearly z-polarized electric field $\varepsilon(t)$ of the form

$$\varepsilon(t) = \varepsilon_0 \sin^2\left(\frac{\pi t}{T}\right)\cos(\omega t + \varphi)$$
$$\text{for } 0 < t < T; \quad \text{otherwise } \varepsilon(t) = 0, \tag{12}$$

where ε_0 is the peak field strength, ω is the optical frequency, T is the pulse duration, and φ is the carrier-envelope phase. The limits of $t_0 \to -\infty$ and $t \to \infty$ in Eq. (8) are replaced by $t_0=0$ and $t=T$, respectively. We impose the boundary condition $\mathbf{A}(T)=0$ on the vector potential so that the canonical momentum $\mathbf{p}_f$ corresponds to the kinetic momentum measured by a detector. [Unless T is an integer multiple of $2\pi/\omega$, the integral of the field $\varepsilon(t)$ from $t_0=0$ to $t=T$, i.e., the difference between $\mathbf{A}(T)$ and $\mathbf{A}(0)$, is nonzero.]

A. Construction of an orbital basis set

We use a set of Gaussian functions of which the exponential parts are given by $\{\exp(-\alpha_{lk}r^2), k=1,\ldots,N_l\}$ to express atomic orbitals of the azimuthal quantum number l. First, we have to construct Gaussian basis functions suitable for the description of the excited state dynamics involved in $|\Phi_i(t)\rangle$. Gaussian basis sets frequently used for the H atom in *ab initio* quantum chemistry calculations, such as the 6-31G(d) basis set [17], are inadequate for the present purpose because they describe the ground state with sufficient accuracy but do not accurately reproduce the energies of excited states. In the present study, the exponents $\{\alpha_{lk}, k=1,\ldots,N_l\}$ for l-type orbitals are generated by means of the optimal even-tempered expansion method proposed by Schmidt and Ruedenberg [24]: the N_l exponents of $\{\alpha_{lk}\}$ are functions of only two adjustable parameters. For various sets of two parameters, we calculated the energies of H. The two parameters are thus optimized to minimize the square errors of the calculated energies of H up to the principal number $n=3$. We employed $12s/12p$ Gaussian functions without contraction; for the s type of optimized orbital, the maximum of $\{\alpha_{l=0,k}, k=1,\ldots,12\}$ is 98 $(1/a_0^2)$ and the minimum is $5.2\times10^{-3}(1/a_0^2)$, where a_0 is the Bohr radius; for the p type of optimized orbital, the maximum of $\{\alpha_{l=1,k}, k=1,\ldots,12\}$ is 7.6 $(1/a_0^2)$ and the minimum is 4.4×10^{-3} $(1/a_0^2)$. Diagonalization of the field-free Hamiltonian with the constructed basis set excellently reproduces the energies of the ground and excited states of H_2^+ (irrespective of the internuclear distance) as well as those of H. The quantitative features of the ionization probabilities and photoelectron spectra of H and H_2^+ did not significantly change when d orbitals were added to the basis set.

B. Enhanced ionization of H_2^+

In the case of molecules, we treat the nuclear degrees of freedom, such as the internuclear distance R of H_2^+, as parameters. It is known that the ionization probability of H_2^+ in a near-infared intense laser field has a peak or peaks between internuclear distances $R=6a_0$ and $R=10a_0$ [12(a)–12(c)]. Enhanced ionization of H_2^+, i.e., a marked increase in the ionization probability at large internuclear distances, is attributed to the fact that the dynamical behavior of the bound electron prior to ionization varies with R [10,11]. It is thus meaningful to examine whether or not the dependence of the ionization probability of H_2^+ on R is accurately reproduced by the present approach designed to include the effects of bound state dynamics. In this subsection, we present the results of calculation of the total ionization probability of H_2^+ as a function of R. The following values are used for the parameters of the applied pulse: $\varepsilon_0=0.05E_h/ea_0$ (peak light intensity $I_0=8.75\times10^{13}$ W/cm^2), $\omega=0.06E_h/\hbar$ (wavelength $\lambda=760$ nm), $T=5.25$ optical cycles ($T=13.3$ fs), and $\varphi=-\pi/2$, where e is the elementary electric charge and E_h is the hartree. The initial state is $1s\sigma_g$. The molecular axis is set to be parallel to the polarization direction z. Then, only σ states are coupled to each other by the dipole interaction with a z-polarized field.

The ionization probabilities of H_2^+ calculated by the present approach are shown in Fig. 1(a); the ionization probabilities are also plotted on a logarithmic scale in Fig. 1(b). For the expansion of $|\Phi_i(t)\rangle$ in Eq. (6), two sets are employed. The first set is the full expansion in which $|\Phi_i(t)\rangle$ is expanded in terms of all the 48 σ states constructed from the prepared basis set of s and p_z orbitals. In the second set, only the initial $1s\sigma_g$ state is used for expansion, i.e., $|\Phi_i(t)\rangle$ is fixed to $1s\sigma_g$ as $|\Phi_i(t)\rangle=\exp[-iE_{1s\sigma_g}(t-t_0)]|\psi_{1s\sigma_g}(t_0)\rangle$. The ionization probabilities obtained from the first and second sets are denoted in Fig. 1 by circles and triangles, respectively. In Fig. 1(a), the values obtained for the two sets are multiplied by a factor of 0.063 (irrespective of the value of R). Since H_2^+ is a one-electron system, we can accurately solve the TDSE by using a grid representation of the wave function [8]. The ionization probabilities obtained this way, regarded as the "exact" or reference values, are denoted by squares in Fig. 1.

The results of the "exact" simulation show that the ionization probability is maximized at $R\approx10a_0$. In addition, there is a rather flat peak around $R=7a_0$. The origins of these

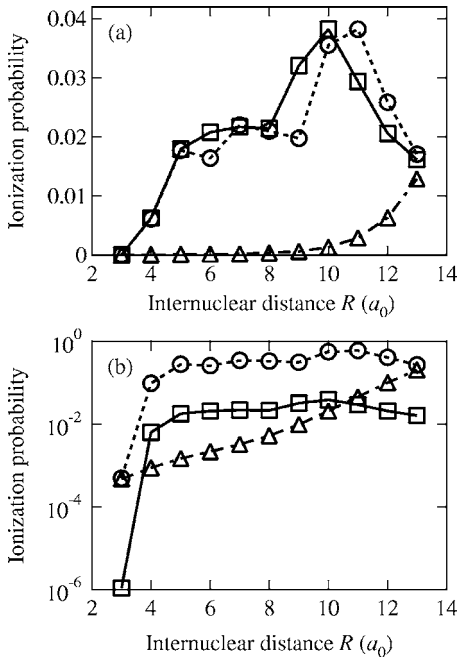

FIG. 1. Ionization probabilities of H_2^+ calculated as a function of the internuclear distance R: (a) liner scale plot; (b) logarithmic scale plot. Parameters for the applied laser pulse in Eq. (12) are as follows: peak light intensity $I_0=8.75\times10^{13}$ W/cm^2, wavelength $\lambda=760$ nm, pulse duration $T=13.3$ fs, and carrier-envelope phase $\varphi=-\pi/2$. The molecular axis is assumed to be parallel to the polarization direction z. The ionization probabilities calculated by an accurate grid point method, regarded as the "exact" or reference values, are denoted by squares. We tested two sets for the expansion of $|\Phi_i(t)\rangle$ in Eq. (6). The first set is the full expansion in which $|\Phi_i(t)\rangle$ is expanded in terms of all the 48 σ states constructed from the prepared basis set of s and p_z orbitals. In the second set, only the initial $1s\sigma_g$ state is used for expansion. The ionization probabilities obtained from the first and second sets are denoted by circles and triangles, respectively. The values obtained from the two sets are multiplied by a factor of 0.063.

two peaks have been clarified in previous papers [25] (see also the discussion below). In the full expansion case of $|\Phi_i(t)\rangle$, the present approach successfully captures the main feature of enhanced ionization of H_2^+, i.e., the above-mentioned double-peak structure appearing in the "exact" case of Fig. 1(a). Although the absolute value of ionization probability in the full expansion case is larger than the "exact" one (we later discuss what causes the overestimation), the overestimation is uniform, about 16-fold, over a wide range of internuclear distance R. Considering the fact that only a small number of basis functions are used in the present approach instead of a huge number of grid points used in the "exact" simulation, the reproduction of the double-peak structure is a bit surprising. To analyze it, in the following, we compare the populations of bound states in $|\Phi_i(t)\rangle$ with those in the entire wave packet $|\Psi_i(t)\rangle$. We use the wave packet obtained by the grid representation method as the "exact" $|\Psi_i(t)\rangle$.

Figure 2 shows the temporal change in the populations of electronic states $1s\sigma_g$, $2p\sigma_u$, and $3d\sigma_g$ for the "exact" simulation and the full expansion case. The internuclear distance

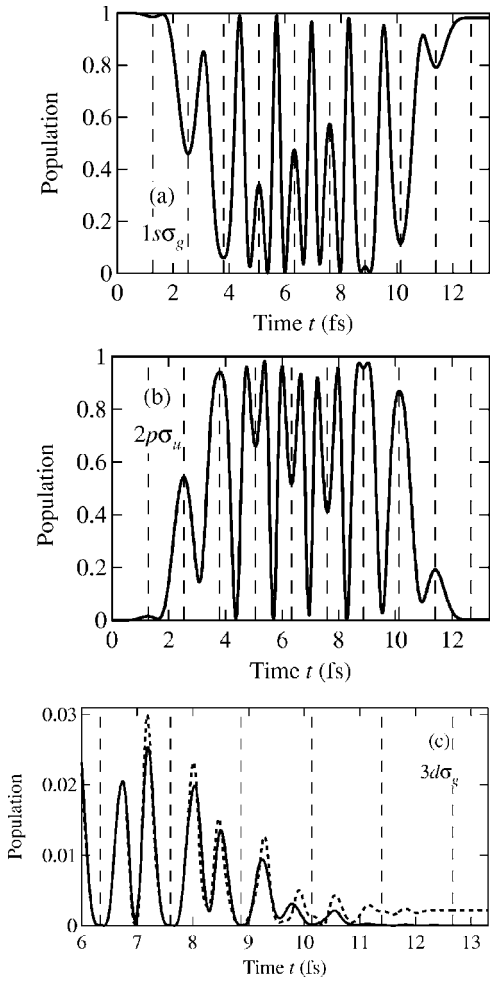

FIG. 2. Temporal change in the populations of electronic states $1s\sigma_g$, $2p\sigma_u$, and $3d\sigma_g$ of H_2^+ at $R=6a_0$. The applied pulse is the same as used in the case of Fig. 1. At $R=6a_0$, $3d\sigma_g$ is the second excited state. The solid lines denote the "exact" populations of the bound states of the entire wave packet $|\Psi_i(t)\rangle$ calculated by a grid point method; the dotted lines denote the populations of the electronic states (expanded in terms of Gaussian functions) of the approximate bound state component $|\Phi_i(t)\rangle$ in the 48 σ state full expansion case. The vertical broken lines indicate moments at which the laser electric field $\varepsilon(t)$ returns to zero.

is fixed at $R=6a_0$, where $3d\sigma_g$ is the second excited state. The solid lines denote the exact populations obtained by projecting each "exact" bound state onto $|\Psi_i(t)\rangle$; the dotted lines denote the projections of the electronic states (expanded in terms of Gaussian functions) onto $|\Phi_i(t)\rangle$. For $1s\sigma_g$ and $2p\sigma_u$, as shown in Figs. 2(a) and 2(b), the populations obtained through the above two procedures are nearly equal to each other. No differences are discernible on the scales of Figs. 2(a) and 2(b). Since the lowest two states $1s\sigma_g$ and $2p\sigma_u$ are coupled to each other by the large transition dipole moment proportional to $R/2$ and the energy of one photon, $\hbar\omega$, is larger than the energy gap $E_{2p\sigma_u}-E_{1s\sigma_g}=0.021E_h$ at $R=6a_0$, a significant amount of population is transferred from $1s\sigma_g$ to $2p\sigma_u$. This process is interpreted as a population transfer due to temporal change in the electric field (field-induced nonadiabatic coupling [10,11]). If the electric

field changes slowly in comparison with the time scale of electronic motion characterized by the reciprocal of the energy gap $E_{2p\sigma_u}-E_{1s\sigma_g}$, i.e., if the process is adiabatic, electron density is transferred between two nuclei according to the optical cycle. In the adiabatic limit, the population of $2p\sigma_u$ returns to zero at the moments of $\varepsilon(t)=0$. This is not the case at large $R>4a_0$, as shown in Fig. 2(b). We have demonstrated in previous papers that electron localization due to field-induced nonadiabatic coupling triggers enhanced ionization. [Another important factor for enhanced ionization of H_2^+ is that the probability of ionization from the populated $2p\sigma_u$ state has a sharp peak (or peaks) in the range between $R=6a_0$ and $R=10a_0$ [10,11].] It should be pointed out that this key population transfer or field-induced electronic dynamics is nearly perfectly reproduced by the present approach.

On the other hand, as shown in Fig. 2(c), the population of $3d\sigma_g$ in $|\Phi_i(t)\rangle$ gradually deviates from that in $|\Psi_i(t)\rangle$. The deviation originates from the fact that the norm of $|\Phi_i(t)\rangle$ in Eq. (6) is conserved, while the total population of bound electronic states in $|\Psi_i(t)\rangle$ is depleted by ionization. Depletion of the populations of excited states due to field-induced ionization is not considered in $|\Phi_i(t)\rangle$. Overall, the deviation in the case of $3d\sigma_g$ is however not so significant. Replacement of the bound state component $|\Psi_{\text{bound}}(t)\rangle \equiv \Sigma_b|\psi_b(t)\rangle\langle\psi_b(t)|\Psi_i(t)\rangle$ by $|\Phi_i(t)\rangle$ in the present approach is justified by the fact that the populations of low-lying key excited states such as $2p\sigma_u$ and $3d\sigma_g$ are well estimated by $|\Phi_i(t)\rangle$.

We notice two features in Fig. 2(c): after the pulse has fully decayed ($t>13.3$ fs), while the population of $3d\sigma_g$ in the exact $|\Psi_i(t)\rangle$ almost vanishes, that in $|\Phi_i(t)\rangle$ takes a nonzero value (though it is small); the population of $3d\sigma_g$ in $|\Phi_i(t)\rangle$ somewhat exceeds the "exact" value around and after the pulse peak. These two features of overestimation become more and more pronounced for the higher excited states such as $3p\sigma_u$. After $t\sim 9$ fs, the $3p\sigma_u$ population in $|\Phi_i(t)\rangle$ is much larger than that in $|\Psi_i(t)\rangle$. The population of a highly excited bound state can be significantly overestimated. Although the populations of the excited states of which the energies are higher than that of $3d\sigma_g$ are very small (<0.005), overestimation of the populations of excited states in the full expansion case leads to the overestimation of the ionization probability as shown in Fig. 1(b).

To investigate the reason for the overestimation of the ionization probability by the present approach, we analyze two quantities: (i) the time-dependent ionization probability $P_I(t)$ defined by the population depletion of the "exact" wave packet in the presence of absorbing boundaries; and (ii) $1-P_{1s\sigma_g}(t)-P_{2p\sigma_u}(t)$, where $P_{1s\sigma_g}(t)$ and $P_{2p\sigma_u}(t)$ are the populations of $1s\sigma_g$ and $2p\sigma_u$, respectively. The $P_I(t)$ is nearly equal to $1-\langle\Psi_{\text{bound}}(t)|\Psi_{\text{bound}}(t)\rangle$, where the bound state component $|\Psi_{\text{bound}}(t)\rangle$ in $|\Psi_i(t)\rangle$ is subject to ionization. The present approach and the grid point method give the same value for $1-P_{1s\sigma_g}(t)-P_{2p\sigma_u}(t)$. As an example, $1-P_{1s\sigma_g}(t)-P_{2p\sigma_u}(t)$ and $P_I(t)$ for the case of $R=6a_0$ are plotted in Fig. 3. For clarity, we divide the bound electronic states into two groups. The first one is Group I consisting of

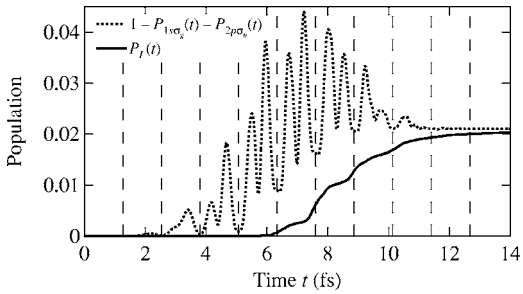

FIG. 3. Time-dependent populations of H_2^+ at $R=6a_0$. The applied pulse is the same as used in the case of Fig. 1. The solid line denotes the time-dependent ionization probability $P_I(t)$ defined by the population depletion of the "exact" wave packet in the presence of absorbing boundaries. The dotted line denotes $1-P_{1s\sigma_g}(t)-P_{2p\sigma_u}(t)$, where $P_{1s\sigma_g}(t)$ and $P_{2p\sigma_u}(t)$ are the populations of the lowest two states $1s\sigma_g$ and $2p\sigma_u$, respectively. The vertical broken lines indicate moments at which the laser electric field $\varepsilon(t)$ returns to zero.

the lowest two electronic states, $1s\sigma_g$ and $2p\sigma_u$. The members of Group II are bound states higher than $2p\sigma_u$. The difference between $1-P_{1s\sigma_g}(t)-P_{2p\sigma_u}(t)$ and $P_I(t)$ is the total population of Group II.

The quantity $1-P_{1s\sigma_g}(t)-P_{2p\sigma_u}(t)$ can be divided into the ionization probability $P_I(t)$ and the total population of Group II. It should be noted in Fig. 3 that whenever the electric field $\varepsilon(t)$ approaches zero, the population of Group II decreases while $P_I(t)$ increases. This indicates that ionization from a created excited state higher than $2p\sigma_u$ is completed almost within one optical cycle. As a result, as shown in Fig. 3, $1-P_{1s\sigma_g}-P_{2p\sigma_u}$ at $t=T$ is nearly equal to the final ionization probability at $t=T$ or $t=\infty$. As mentioned, $1-P_{1s\sigma_g}(t)-P_{2p\sigma_u}(t)$ obtained from $|\Phi_i(t)\rangle$ by the present approach is equal to the "exact" one in Fig. 3. However, in the case of the present approach, the quantity $1-P_{1s\sigma_g}(t)-P_{2p\sigma_u}(t)$ does not include any depletion of the bound state population due to ionization and hence represents the total population of Group II in $|\Phi_i(t)\rangle$. Here, we define an artificial bound state component $|\Phi_i^h(t)\rangle$ by $|\Phi_i^h(t)\rangle \equiv |\Phi_i(t)\rangle - |\Psi_{\text{bound}}(t)\rangle$. The component $|\Phi_i^h(t)\rangle$ contains excited states of Group II that are higher than those involved in $|\Psi_{\text{bound}}(t)\rangle$ in addition to those in $|\Psi_{\text{bound}}(t)\rangle$.

The wave packet $|\Phi_i(t)\rangle$ is thus expressed as

$$|\Phi_i(t)\rangle = |\Psi_{\text{bound}}(t)\rangle + |\Phi_i^h(t)\rangle. \tag{13}$$

When Eq. (13) is inserted into Eq. (8), the second term in Eq. (13), i.e., $|\Phi_i^h(t)\rangle$, causes overestimation of the ionization probability. We expect that the overlap $\langle\Phi_i^h(t)|\Psi_{\text{bound}}(t)\rangle \sim 0$ because many bound states are commonly involved in $|\Psi_{\text{bound}}(t)\rangle$ and $|\Phi_i^h(t)\rangle$ so that the sum of the individual overlaps is close to zero. The total population of the highly lying bound states of $|\Phi_i^h(t)\rangle$ (which in the "real" situation are subject to prompt ionization) is then nearly given by the ionization probability $P_I(t)$. (Note that $\langle\Psi_{\text{bound}}(t)|\Psi_{\text{bound}}(t)\rangle = 1-P_I(t)$.) We found that $P_I(t)$ is well approximated by the form $P_I(t)=P_I(T)f(t)$, where $f(t)$ is independent of the inter-

nuclear distance R. Moreover, the ionization rates of higher excited states in $|\Phi_i^h(t)\rangle$ are overwhelmingly large and are uniform irrespective of R. The contribution of $|\Phi_i^h(t)\rangle$ to the calculated ionization probability is thus simply proportional to $P_I(T)$. Presumably, this is the reason why the overestimation of the ionization probability (16-fold) is uniform over a wide range of R. This uniformity of the overestimation also contributes to the reproduction of the double-peak structure in the R dependence of the ionization probability.

To confirm that the overestimated populations of excited states lead to the overestimation of the ionization probability, we introduced phenomenological tunneling rates for individual bound states $\{|\psi_b(t_0)\rangle\}$ into Eq. (7). The tunneling rate for $|\psi_b(t_0)\rangle$ was assumed to take a simple form as $w \exp[-4\sqrt{2I_{p,b}}/3|\varepsilon(t)|]$, where $I_{p,b}$ is the ionization potential for $|\psi_b(t_0)\rangle$. The common preexponential factor w was determined so that the populations of highly excited states in the calculated $|\Phi_i(t)\rangle$ also change temporally in the same manner as the exact ones in $|\Psi_{\text{bound}}(t)\rangle$ decrease owing to ionization. Then, as expected, the ionization probability calculated using Eq. (8) was reduced to about one-tenth, being just as large as the exact ionization probability.

The $1s\sigma_g$ single-state expansion fails to reproduce the double-peak structure, as shown in Fig. 1. In the case of the $1s\sigma_g$ single-state expansion, the calculated ionization probability monotonically increases with increase in R. The increase in the ionization probability in the range up to $R \sim 8a_0$ is ascribed simply to the sharp decrease in the ionization potential. Further monotonic increase in the ionization probability at large $R > 8a_0$ is due to the substantial defect that the effects of intramolecular electronic dynamics such as population transfer to $2p\sigma_u$ are not taken into account at all in the $1s\sigma_g$ single-state expansion case.

C. Photoelectron spectrum of H

Recent advanced time-of-flight measurement of photoelectrons and ions created by laser fields has enabled one to achieve a momentum resolution better than $0.02\ \hbar/a_0$ [26]. Observed high-resolution momentum distributions have attracted attention owing to their intriguing structures. For example, the measured distribution of the photoelectron (or ion) momentum perpendicular to the polarization direction of an applied intense laser field displays a sharp cusp-like peak at the transverse momentum $p_\perp = 0$ with a broad low intensity component. This feature of the transverse momentum distribution is observed for single ionization of noble gas atoms and H_2 and considered a general phenomenon, irrespective of the systems [19].

Dimitriou *et al.* [27] performed a full quantum calculation of an H atom and a quasiclassical trajectory Monte Carlo calculation including tunneling effects (CTMC-T). In both calculations, a cusp structure in the transverse momentum distribution is reproduced. When the Coulomb interaction for the outgoing trajectories is switched off in CTMC-T calculation, the transverse momentum distribution reverts to a Gaussian-like distribution with a maximum at $p_\perp = 0$, as predicted by standard tunneling theory [28]. In a very recent study, Rudenko *et al.* performed calculations using the KFR S-matrix approach [19]. The "cusp" appears when a Coulomb-Volkov state is used as a final electron state and it does not appear when a Volkov state is used. Because of this fact, they have attributed its origin to the long-range Coulomb interaction between the emitted electron and the remaining ion core, i.e., the final-state effects due to two-body Coulomb interaction. They have also attributed the broad low intensity component in the transverse momentum distribution to "rescattering" [29].

Since in the present version of our approach a plane wave or Volkov state is employed as the final state, it cannot reproduce the "cusp" originating from the final-state Coulomb interaction. It is however interesting to apply the present version to the calculation of the photoelectron momentum distribution of H to clarify the performance or limitation of the present version. For an applied pulse, we adopt the same parameters as Dimitriou *et al.*: $\varepsilon_0 = 0.075 E_h/ea_0$ ($I_0 = 2.0 \times 10^{14}$ W/cm^2), $\omega = 0.05 E_h/\hbar$ ($\lambda = 910$ nm), $T = 4$ optical cycles ($T = 12.2$ fs), and $\varphi = 0$.

Distributions of transverse momentum $p_\perp = p_x$ for three cases are shown in Fig. 4(a). The three-dimensional distribution is integrated over the other transverse momentum p_y and the longitudinal momentum $p_\parallel = p_z$, as in [19,27]. The solid line denotes the transverse momentum distribution in the case of the full expansion of $|\Phi_i(t)\rangle$, i.e., where $|\Phi_i(t)\rangle$ is expanded in terms of all 24 states constructed from the present basis set of s and p_z types of Gaussian functions. The dotted line indicates the transverse momentum distribution for the case in which $|\Phi_i(t)\rangle$ is expanded in terms of the lowest seven states of the field-free Hamiltonian. The photoelectron yield is multiplied by a factor of 1.6 to fit the maximum value at $p_\perp = 0$ to that in the full expansion case. The dash-dotted line denotes the transverse momentum distribution for the expansion of $|\Phi_i(t)\rangle$ in terms of the initial state $1s$ orbital alone, i.e., $|\Phi_i(t)\rangle = \exp[-iE_{1s}(t-t_0)]|\psi_{1s}(t_0)\rangle$. The multiplication factor is 30. The distributions for negative $p_\perp$ are the mirror images of those for positive $p_\perp$.

For the full expansion and seven-state expansion cases, the peak of the distribution at $p_\perp = 0$ is as sharp as that in the CTMC-T or the full quantum calculation by Dimitriou *et al.* However, the second order differential coefficients of the transverse momentum distributions at $p_\perp = 0$ in Fig. 4(a) are all negative, whereas the second order differential coefficient of a "cusp" is positive. The distribution for the one-state expansion of $|\Phi_i(t)\rangle = \exp[-iE_{1s}(t-t_0)]|\psi_{1s}(t_0)\rangle$ shows an even rounder peak at $p_\perp = 0$. No "cusps" are reproduced in the present results.

Analysis of the present results, however, provides a clue to understanding field-induced dynamics of an electron in a Coulomb field. Figure 4(a) has shown that the width of the peak at $p_\perp = 0$ becomes narrower if excited states are included in $|\Phi_i(t)\rangle$. The half width at half maximum (HWHM) in the $1s$ single-state expansion case is larger than that of the seven-state or full expansion case where excited states are involved in the time-evolving wave packet $|\Phi_i(t)\rangle$. The narrowing of the peak can be explained by expansions in terms of $1s$, $2s$, and $2p_z$. Using these three states, we calculated transverse momentum distributions. The thin solid line shown in Fig. 4(b) denotes the distribution for the

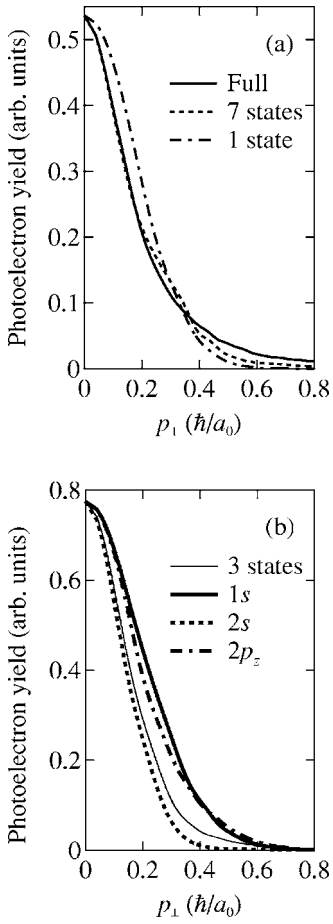

FIG. 4. Distributions of transverse momentum $p_\perp = p_x$ of H (integrated over the other transverse momentum p_y and $p_\parallel = p_z$) based on the present theoretical treatment. Parameters for the z-polarized applied field are as follows: peak light intensity $I_0 = 2.0 \times 10^{14}$ W/cm^2, wavelength $\lambda = 910$ nm, pulse duration $T = 12.2$ fs, and carrier-envelope phase $\varphi = 0$. The solid line in (a) denotes the transverse momentum distribution in the case of the full 24-state expansion of $|\Phi_i(t)\rangle$ constructed from the present basis set of s and p_z orbitals. The dotted and dash-dotted lines in (a) indicate the transverse momentum distributions for the seven-state and $1s$ single-state expansion cases, respectively. The yields in the seven-state and $1s$ single-state expansion cases are multiplied by 1.6 and 30, respectively, so that the scaled peak values at $p_\perp = 0$ are the same for the three cases. The thin solid line in (b) denotes the distribution for the three-state expansion $|\Phi_i'(t)\rangle = c_{1s}(t)|\psi_{1s}(t)\rangle + c_{2s}(t)|\psi_{2s}(t)\rangle + c_{2p_z}(t)|\psi_{2p_z}(t)\rangle$. The bold solid line in (b) denotes the momentum distribution for the case in which only the $1s$ component in $|\Phi_i'(t)\rangle$ is used for the calculation, i.e., $c_{2s}(t) = c_{2p_z}(t) = 0$. The dotted and dash-dotted lines in (b) denote the momentum distributions for the $2s$ and $2p_z$ components, respectively. The photoelectron yields in the $1s$, $2s$, and $2p_z$ component cases are multiplied by 48, 2.5, and 2.4, respectively.

three-state expansion $|\Phi_i'(t)\rangle = c_{1s}(t)|\psi_{1s}(t)\rangle + c_{2s}(t)|\psi_{2s}(t)\rangle + c_{2p_z}(t)|\psi_{2p_z}(t)\rangle$. The bold solid line denotes the momentum distribution for the case in which only the $1s$ component in $|\Phi_i'(t)\rangle$ is used for the calculation, i.e., $c_{1s}(t) \neq 0$ and $c_{2s}(t) = c_{2p_z}(t) = 0$. The dotted and dash-dotted lines denote the momentum distributions for the $2s$ and $2p_z$ components in $|\Phi_i'(t)\rangle$, respectively. Each curve is multiplied to fit the peak values to that in the three-state expansion case. The multiplication factors for the $1s$, $2s$, and $2p_z$ component cases are 48, 2.5, and 2.4, respectively.

The width of the transverse momentum distribution in the $2s$ component case is the narrowest. The momentum distribution in a single-component case reflects the width in the momentum representation of the corresponding field-free wave function. For example, the shape of the momentum distribution curve in the $2s$ component case is nearly identical to that in the $2s$ state expansion case of $|\Phi_i(t)\rangle = \exp[-iE_{2s}(t-t_0)]|\psi_{2s}(t_0)\rangle$ and also identical to the momentum representation of the $2s$ wave function itself. The radial wave function of an H atom becomes broader as the principal number n increases. The width of the wave function in the transverse direction x or y depends also on the azimuthal and magnetic quantum numbers. Compared to the transverse spatial width of the $2s$ wave function, that of $2p_z$ is small (because of its unisotropic spherical harmonic function); the order of the transverse width is $1s < 2p_z < 2s$. Hence, in transverse momentum space, the width of $2s$ is the smallest among the three states.

In the low-momentum domain of $p_\perp < 0.2\hbar/a_0$, as shown in Fig. 4(b), the peak width of the photoelectron yield curve in the three-state expansion is as narrow as the width in the $2s$ component case; the relative photoelectron yield curve in the three-state expansion case is closer to that in the $2s$ component case than that in the $2p_z$ component case, although the $2s$ and $2p_z$ components in the three-state expansion $|\Phi_i'(t)\rangle$ have almost the same magnitude. The proximity of the three-state expansion case to the $2s$ component case in the low-momentum domain is attributed to the interference originating from a linear combination of the three states in $|\Phi_i'(t)\rangle$, i.e., the effects of motion of the wave packet. In fact, the interference between the $2s$ and $2p_z$ components is important. We have confirmed that the relative yield curve in the three-state expansion case is reproduced by the linear combination of the two components in $|\Phi_i'(t)\rangle$, i.e., $c_{2s}(t)|\psi_{2s}(t)\rangle + c_{2p_z}(t)|\psi_{2p_z}(t)\rangle$.

In the low-momentum domain, the relative photoelectron yield curves for the three-state, seven-state, and full expansion cases are nearly the same; i.e., the main feature of the yield curve is governed by the $2s$ and $2p_z$ components in $|\Phi_i(t)\rangle$ irrespective of the presence of the other components. The importance of the $2s$ and $2p_z$ states comes from the fact that the populations of the $2s$ and $2p_z$ states are much larger than those of the other excited states.

However we notice that the distribution in the high-momentum domain ($p_\perp > 0.4\hbar/a_0$) depends on how many excited states are taken into account besides the $2s$ and $2p_z$ states. Transverse momentum distributions for various cases are plotted on a logarithmic scale in Fig. 5. The dash-dotted, dotted, and solid bold lines represent the momentum distributions for the three-state, seven-state, and full expansion cases, respectively. The solid and broken thin lines represent the momentum distributions for $1s$ and $2s$ single-state expansions, respectively. (In the case of the $2s$ single-state expansion, the initial state is assumed to be $2s$.) The multiplication factors for fitting to the peak value in the full expansion case

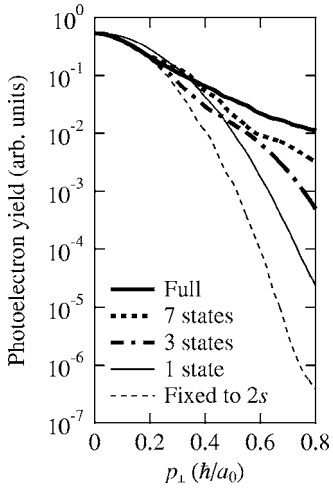

FIG. 5. Transverse momentum distributions of H on a logarithmic scale. The applied pulse is the same as used in the case of Fig. 4. The dash-dotted, dotted, and solid bold lines represent the momentum distributions for the three-state, seven-state, and full expansion cases, respectively. The solid and broken thin lines represent the momentum distributions for 1*s* and 2*s* single-state expansions, respectively. The photoelectron yields in the three-state and seven-state expansion cases are multiplied by 0.69 and 1.6, respectively; those in the 1*s* and 2*s* single-state expansion cases are multiplied by 30 and 4.1×10^{-3}, respectively.

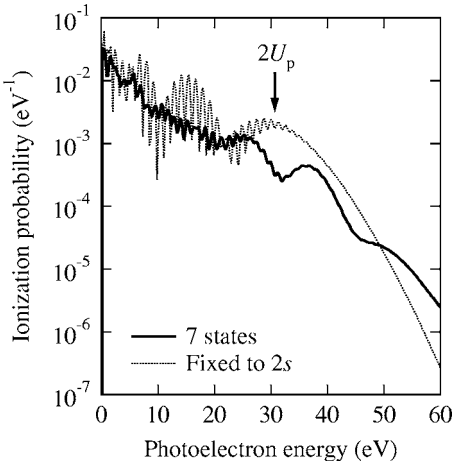

FIG. 6. Photoelectron spectra of H. The applied pulse is the same as used in the case of Fig. 4. The bold and thin lines correspond to the seven-state and 2*s* single-state expansion cases, respectively. (The values in the latter case are multiplied by a factor of 5.0×10^{-3}.) Above-threshold ionization (ATI) peaks appear at intervals of photon energy $\hbar\omega$. The intensity in the single-state expansion case falls off beyond the energy of $2U_p\sim30.6$ eV, while an extended plateau beyond $2U_p$ appears in the seven-state expansion case (where U_p is the ponderomotive energy).

are as follows: 0.69 for the three-state expansion, 1.6 for the seven-state expansion, 30 for the 1*s* single-state expansion, and 4.1×10^{-3} for the 2*s* single-state expansion, respectively. The distribution curves for the multistate expansion cases change their slopes around $p_\perp=0.4\hbar/a_0-0.6\hbar/a_0$. The existence of this broad component is due to the dynamical effects of the time-evolving wave packet because the distribution for a single-state expansion case exhibits a monotonic decrease as shown in Fig. 5 and the slope of the tail beyond $p_\perp=0.6\hbar/a_0$ becomes gentler as the number of excited states is increased. This finding is consistent with the conclusion of Rudenko *et al.* that the broad low intensity component in the transverse momentum distribution is due to "rescattering" [19]. Although $|\Phi_i(t)\rangle$ covers only a limited configuration space, the mixing of bound excited states in $|\Phi_i(t)\rangle$ enables the wave packet to mimic the effects of "on the way out" scattering [7(b)] or "rescattering."

Photoelectron spectra (energy distributions) calculated for the same pulse as in the cases of Figs. 4 and 5 are plotted in Fig. 6. The bold and thin lines correspond to the seven-state and 2*s* single-state expansion cases, respectively. (The values in the latter case are multiplied by a factor of 5.0×10^{-3}.) In both cases, above-threshold ionization (ATI) peaks appear at intervals of photon energy $\hbar\omega$, although the peaks are much sharper in the latter case. According to a classical model, if an electron does not interact with the remaining ion after the first step of ionization (direct ionization), the photoelectron intensity has a cutoff around the energy of $2U_p$, where $U_p(=\varepsilon_0^2/4\omega^2)$ is the ponderomotive energy (~15.3 eV in this case). As expected, the intensity in the single-state expansion case falls off beyond ~30 eV. In contrast, an extended plateau beyond $2U_p$ appears in the seven-state expansion case, which indicates that the effects of dynamical motion of the wave packet are indeed taken into account in the present approach, albeit in an incomplete fashion.

IV. CONCLUSIONS

In this study, we combined a wave-packet propagation method for bound electronic state dynamics with the intense-field *S*-matrix theory to calculate the ionization probability of an atom or a molecule in an intense near-infrared laser field. Our approach is applicable to pulse excitation cases. To begin with, the wave packet composed of only bound states, $|\Phi_i(t)\rangle$, is introduced. Then, the entire wave function $|\Psi_i(t)\rangle$ in the integral kernel in the post form of the solution of the time-dependent Schrödinger equation, Eq. (3), is approximated by $|\Phi_i(t)\rangle$; moreover, the bound state component of $|\Psi_i(t)\rangle$ is replaced by $|\Phi_i(t)\rangle$ in the evaluation stage of the *S*-matrix element of Eq. (5). In the present method, the advantage of the use of the post form of $|\Psi_i(t)\rangle$ is twofold. First, the effects of both Coulomb field and radiation field on the bound electron(s) are reproduced by $|\Phi_i(t)\rangle$ in a nonperturbative way. Second, the effects of a radiation field on a freed electron are also taken into account in a nonperturbative way as in the KFR theory.

The present method can quantitatively reproduce the dependence of the ionization probability of H_2^+ on the internuclear distance *R*, i.e., the double-peak structure at large *R* obtained by the accurate grid propagation method, even if only a small number (~48) of Gaussian basis functions are used in the expansion of $|\Phi_i(t)\rangle$. The reproduction of the double-peak structure establishes the conclusion that the process of field-induced nonadiabatic electronic dynamics associated with population transfer from $1s\sigma_g$ to $2p\sigma_u$ induces

enhanced ionization. Population transfer from $1s\sigma_g$ to $2p\sigma_u$ is nearly perfectly reproduced by the present approach. We confirmed that the populations of low-lying key excited states such as $2p\sigma_u$ and $3d\sigma_g$ are well estimated by $|\Phi_i(t)\rangle$. However, the populations of the higher excited states are significantly overestimated, which leads to the overestimation of the absolute value of the total ionization probability. The next step to improve the present method is to consider depletion of the populations of excited states due to field-induced ionization by imposing an absorbing boundary on $|\Phi_i(t)\rangle$.

We also applied the method to calculate the photoelectron momentum distribution of H in an intense near-infrared field. If the lowest three states ($1s$, $2s$, and $2p_z$) or more states are included in $|\Phi_i(t)\rangle$, the peak of the transverse momentum distribution at $p_\perp=0$ is as sharp as that in the CTMC-T or the full quantum calculation by Dimitriou *et al.* [27]. However, "cusps" at $p_\perp=0$ do not appear. This indirectly supports the conclusion by Rudenko *et al.* [19] that the effects of the long-range Coulomb interaction in the final state are responsible for the experimentally observed cusp structure because the present version of our approach employs a plane wave or Volkov state as the final state. In the low-momentum domain of $p_\perp<0.2\hbar/a_0$, the main feature of the yield curve is governed by the $2s$ and $2p_z$ components in $|\Phi_i(t)\rangle$ irrespective of the presence of the other components. The importance of the $2s$ and $2p_z$ states comes from the fact that the populations of the $2s$ and $2p_z$ states are much larger than those of the other excited states.

The distribution curves for multistate expansion cases change their slopes around $p_\perp=0.4\hbar/a_0-0.6\hbar/a_0$. The existence of this broad low intensity component is due to the dynamical motion of the time-evolving wave packet $|\Phi_i(t)\rangle$. This finding is consistent with the conclusion of Rudenko *et al.* that the broad low intensity component in the transverse momentum distribution is due to "rescattering." A signature of "rescattering" is also printed in the photoelectron energy spectrum; an extended plateau beyond $2U_p$ appears. Although $|\Phi_i(t)\rangle$ covers only a limited configuration space, it turned out that the mixing of bound excited states in $|\Phi_i(t)\rangle$ provides a proper nonperturbative description of electronic dynamics in the presence of both Coulomb and laser fields.

One of the advantages of this approach is that only a small number of basis functions are required. We are applying it to two-electron systems such as the H_2 molecule or He to investigate the effects of electron correlation. The effects of electron correlation on excited state dynamics are not fully taken into account even in current time-dependent density functional theory [30]. We expect that the present approach designed for the reproduction of bound excited state dynamics can capture the feature of enhanced ionization of polyatomic multielectron molecules.

ACKNOWLEDGMENTS

M.K. and H.K. are grateful to Dr. A. Becker, Dr. A. Rudenko, Dr. I. Kawata, Dr. Y. Teranishi, and Professor Y. Ohtsuki for their valuable discussions. H.K. and F.H.M.F. wish to express their gratitude for the encouragement received from Professor K. Yamanouchi. This work was supported in part by a grant-in-aid for scientific research (Grant No. 16350001) and a grant-in-aid for scientific research on priority areas, "Control of Molecules in Intense Laser Field" (Area No. 419) from the Ministry of Education, Culture, Sports, Science and Technology, Japan. We also acknowledge the support of the JSPS Core-to-Core Program on "Ultrafast Intense Laser Science."

APPENDIX: INTEGRALS BETWEEN HYBRID GF-PW BASIS FUNCTIONS

The matrix elements between a plane wave (PW) and a Gaussian function (GF) can be expressed by more general forms, namely, matrix elements between hybrid GF-PW basis functions. There is much work on the integrals between Gaussian functions [23]. McMurchie and Davidson (MD) presented a sophisticated algorithm to evaluate the integrals between Gaussian functions [31]. The MD algorithm takes advantage of the property of the Hermite polynomial to expand the integral in terms of auxiliary functions. Tachikawa and Shiga (TS) applied the MD algorithm to the evaluation of matrix elements between hybrid GF-PW basis functions [32]. In this Appendix, we thoroughly follow the original MD algorithm and derive, in a stepwise manner, recursion formulas for obtaining the overlap and nuclear attraction (binding potential) integrals involving hybrid GF-PWs. We also outline computational algorithms to evaluate the integrals in auxiliary functions involved in the recursion formulas.

Expansion of integrals

A hybrid GF-PW basis function χ_A is characterized by a positive exponent α_A, central position $\mathbf{R}_A$, and central momentum $\mathbf{p}_A$:

$$\chi_A = \prod_{k=x,y,z} (r_k - R_{Ak})^{n_{Ak}} \times \exp[-\alpha_A(\mathbf{r}-\mathbf{R}_A)^2]\exp[i\mathbf{p}_A\cdot(\mathbf{r}-\mathbf{R}_A)], \quad \text{(A1)}$$

where $\mathbf{r}$ denotes the electronic coordinate and n_{Ak} are nonnegative integers. The product of two hybrid GF-PWs is given by

$$\chi_A^*\chi_B = E_{AB}\prod_{k=x,y,z}(r_k-R_{Ak})^{n_{Ak}}(r_k-R_{Bk})^{n_{Bk}} \times \exp[-\alpha_P(\mathbf{r}-\mathbf{P})^2 + i\mathbf{pr}], \quad \text{(A2)}$$

where

$$\alpha_P \equiv \alpha_A+\alpha_B, \quad \mathbf{P} \equiv \frac{\alpha_A\mathbf{R}_A+\alpha_B\mathbf{R}_B}{\alpha_P}, \quad \mathbf{p}\equiv\mathbf{p}_B-\mathbf{p}_A,$$

$$E_{AB} \equiv \exp\left[-\frac{\alpha_A\alpha_B(\mathbf{R}_A-\mathbf{R}_B)^2}{\alpha_P} + i(\mathbf{p}_A\mathbf{R}_A-\mathbf{p}_B\mathbf{R}_B)\right]. \quad \text{(A3)}$$

Following the procedure by MD, we introduce the function Λ_{N_k} as

$$\Lambda_{N_k}(r_k - P_k;\alpha_P)\exp[-\alpha_P(\mathbf{r}-\mathbf{P})^2] = \left(\frac{\partial}{\partial P_k}\right)^{N_k}\exp[-\alpha_P(\mathbf{r}-\mathbf{P})^2], \tag{A4}$$

where N_k are integers. From the above definition, Λ_{N_k} is related to the Hermite polynomial H_{N_k} by

$$\Lambda_{N_k}(r_k - P_k;\alpha_P) = \alpha_P^{N_k/2} H_{N_k}[\alpha_P^{1/2}(r_k - P_k)]. \tag{A5}$$

The Hermite polynomials are defined as

$$H_{N_k}(u) \equiv (-1)^{N_k}\exp(u^2)\frac{d^{N_k}}{du^{N_k}}\exp(-u^2), \tag{A6}$$

which obey the recursion relation

$$uH_{N_k}(u) = N_k H_{N_k-1}(u) + \tfrac{1}{2}H_{N_k+1}(u). \tag{A7}$$

We can thus obtain the following recursion formula for $\Lambda_{N_k}(r_k - P_k;\alpha_P)$ by inserting the relation of Eq. (A5) into Eq. (A7):

$$(r_k - R_{Ak})\Lambda_{N_k} = N_k\Lambda_{N_k-1} + (P_k - R_{Ak})\Lambda_{N_k} + \frac{1}{2\alpha_P}\Lambda_{N_k+1}. \tag{A8}$$

Let us revert to Eq. (A2) and expand the preexponential polynomials as follows:

$$(r_k - R_{Ak})^{n_{Ak}}(r_k - R_{Bk})^{n_{Bk}} = \sum_{N_k=0}^{n_{Ak}+n_{Bk}} d_{N_k}^{n_{Ak},n_{Bk}}\Lambda_{N_k}(r_k - P_k;\alpha_P). \tag{A9}$$

From Eq. (A8), one obtains the recursion relations for the coefficient $d_{N_k}^{n_{Ak},n_{Bk}}$

$$d_{N_k}^{n_{Ak}+1,n_{Bk}} = \frac{1}{2\alpha_P}d_{N_k-1}^{n_{Ak},n_{Bk}} + (P_k - R_{Ak})d_{N_k}^{n_{Ak},n_{Bk}} + (N_k+1)d_{N_k+1}^{n_{Ak},n_{Bk}}, \tag{A10a}$$

$$d_{N_k}^{n_{Ak},n_{Bk}+1} = \frac{1}{2\alpha_P}d_{N_k-1}^{n_{Ak},n_{Bk}} + (P_k - R_{Bk})d_{N_k}^{n_{Ak},n_{Bk}} + (N_k+1)d_{N_k+1}^{n_{Ak},n_{Bk}}, \tag{A10b}$$

with the initial condition $d_0^{00}=1$. All the coefficients are determined by Eqs. (A10a) and (A10b). Equations (A10a) and (A10b) have already been derived by MD or TS.

The expansion (A9) crucially simplifies the calculation scheme for the matrix elements between hybrid GF-PWs by converting $(r_k - R_{Ak})^{n_{Ak}}(r_k - R_{Bk})^{n_{Bk}}$ into a sum of derivatives of $\exp[-\alpha_P(\mathbf{r}-\mathbf{P})^2]$ with respect to P_k. Differentiations with respect to P_k can be carried out outside of the integral over $\mathbf{r}$. Hence, the matrix element of a physical quantity $\theta(\mathbf{r})$ between hybrid GF-PWs can be expressed as

$$\langle\chi_A|\theta|\chi_B\rangle = E_{AB}\sum_{N_x=0}^{n_{Ax}+n_{Bx}}\sum_{N_y=0}^{n_{Ay}+n_{By}}\sum_{N_z=0}^{n_{Az}+n_{Bz}} d_{N_x}^{n_{Ax},n_{Bx}}d_{N_y}^{n_{Ay},n_{By}}d_{N_z}^{n_{Az},n_{Bz}} \times [N_xN_yN_z|\theta], \tag{A11}$$

where $[N_xN_yN_z|\theta]$ are given by

$$[N_xN_yN_z|\theta] \equiv \prod_{k=x,y,z}\left(\frac{\partial}{\partial P_k}\right)^{N_k}\int d\mathbf{r}\,\theta(\mathbf{r}) \times\exp[-\alpha_P(\mathbf{r}-\mathbf{P})^2 + i\mathbf{pr}]. \tag{A12}$$

The problem is thus recast into the evaluation of $[N_xN_yN_z|\theta]$ for all the allowed values of (N_x,N_y,N_z). By completing the square on the exponential in Eq. (A12), one obtains

$$[N_xN_yN_z|\theta] = \exp\left(-\frac{p^2}{4\alpha_P} + i\mathbf{pP}\right)\prod_{k=x,y,z}\left(ip_k + \frac{\partial}{\partial P_k}\right)^{N_k} \times\int d\mathbf{r}\,\theta(\mathbf{r})\exp[-\alpha_P(\mathbf{r}-\tilde{\mathbf{P}})^2], \tag{A13}$$

where

$$\tilde{\mathbf{P}} \equiv \mathbf{P} + i\frac{\mathbf{p}}{2\alpha_P}. \tag{A14}$$

In the following subsections, we derive the formulas of $[N_xN_yN_z|\theta]$ for the overlap and nuclear attraction integrals.

Overlap integrals

The overlap integral is easily derived by setting $\theta(\mathbf{r})=1$ in Eq. (A13):

$$[N_xN_yN_z|1] = \exp\left(-\frac{p^2}{4\alpha_P} + i\mathbf{pP}\right)\left(\frac{\pi}{\alpha_P}\right)^{3/2}\prod_{k=x,y,z}(ip_k)^{N_k}. \tag{A15}$$

Nuclear attraction integrals

In the case of the nuclear attraction integral, $\theta(\mathbf{r})$ is replaced by $r_C^{-1} \equiv |\mathbf{r}-\mathbf{C}|^{-1}$, where $\mathbf{C}$ denotes the nuclear coordinate. According to Boys [33], the integral in Eq. (A13) for the nuclear attraction integral is given by

$$\int d\mathbf{r}\frac{1}{r_C}\exp[-\alpha_P(\mathbf{r}-\tilde{\mathbf{P}})^2] = \frac{2\pi}{\alpha_P}F_0(T), \tag{A16}$$

where

$$T \equiv \alpha_P(\tilde{\mathbf{P}} - \mathbf{C})^2, \quad F_0(T) = \int_0^1 du\,\exp(-Tu^2). \tag{A17}$$

Here, we define the auxiliary function $R_{N_xN_yN_z}$ as

$$R_{N_xN_yN_z} \equiv \prod_{k=x,y,z}\left(ip_k + \frac{\partial}{\partial P_k}\right)^{N_k}F_0. \tag{A18}$$

The nuclear attraction integral is then written as

$$[N_xN_yN_z|r_C^{-1}] = \exp\left(-\frac{p^2}{4\alpha_P} + i\mathbf{pP}\right)\frac{2\pi}{\alpha_P}R_{N_xN_yN_z}(T). \tag{A19}$$

To derive recursion formulas for the evaluation of $R_{N_xN_yN_z}$, we introduce two sets of functions. We first define the complex Hermite polynomials $H^c_{N_k}$ by treating the argument in Eq. (A6) as a complex number. Since $H^c_{N_k}$ are obtained simply by extending the argument of H_{N_k} to the complex number plane, $H^c_{N_k}$ satisfy the same recursion relation as in Eq. (A7). We also define more general complex functions G_{N_k} as

$$G_{N_k}(v;\beta) \equiv (-1)^{N_k}\exp(v^2)\left(i\beta + \frac{d}{dv}\right)^{N_k}\exp(-v^2), \tag{A20}$$

where v is a complex number. Note that setting $\beta=0$ reduces G_{N_k} to the complex Hermite polynomial $H^c_{N_k}$. Using the binomial theorem, we can expand G_{N_k} in terms of $H^c_{N_k}$:

$$G_{N_k}(v;\beta) = \sum_{m=0}^{N_k}\binom{N_k}{m}(-i\beta)^{N_k-m}H^c_m(v). \tag{A21}$$

Then the following recursion relation for G_{N_k} is derived from that for $H^c_{N_k}$:

$$\left(v - \frac{i\beta}{2}\right)G_{N_k} = N_kG_{N_k-1} + \frac{1}{2}G_{N_k+1}. \tag{A22}$$

By using G_{N_k}, we can express $R_{N_xN_yN_z}$ as the following integral form:

$$R_{N_xN_yN_z}(T) = \int_0^1 du\exp(-Tu^2)\prod_{k=x,y,z}(-\alpha_P^{1/2}u)^{N_k} \times G_{N_k}\left[\alpha_P^{1/2}(\tilde{P}_k - C_k)u; \frac{p_k}{\alpha_P^{1/2}u}\right]. \tag{A23}$$

A way to evaluate $R_{N_xN_yN_z}$ is found by introducing the more general integrals as

$$R_{N_xN_yN_z\,j}(T) = (-2\alpha_P)^j\int_0^1 duu^{2j}\exp(-Tu^2)\prod_{k=x,y,z} \times(-\alpha_P^{1/2}u)^{N_k}G_{N_k}\left[\alpha_P^{1/2}(\tilde{P}_k - C_k)u; \frac{p_k}{\alpha_P^{1/2}u}\right]. \tag{A24}$$

The recursion formulas for $R_{N_xN_yN_z\,j}$ can be derived from Eq. (A22):

$$R_{N_x+1N_yN_z\,j} = N_xR_{N_x-1N_yN_z\,j+1} + ip_xR_{N_xN_yN_z\,j} + (\tilde{P}_x - C_x)R_{N_xN_yN_z\,j+1}, \tag{A25a}$$

$$R_{N_xN_y+1N_z\,j} = N_yR_{N_xN_y-1N_z\,j+1} + ip_yR_{N_xN_yN_z\,j} + (\tilde{P}_y - C_y)R_{N_xN_yN_z\,j+1}, \tag{A25b}$$

$$R_{N_xN_yN_z+1j} = N_xR_{N_xN_yN_z-1j+1} + ip_zR_{N_xN_yN_z\,j} + (\tilde{P}_z - C_z)R_{N_xN_yN_z\,j+1}. \tag{A25c}$$

All of the $R_{N_xN_yN_z}(=R_{N_xN_yN_z0})$ are thus generated from Eqs. (A25a)–(A25c) and the initial condition

$$R_{000j} = (-2\alpha_P)^jF_j, \tag{A26}$$

where

$$F_j(T) = \int_0^1 duu^{2j}\exp(-Tu^2). \tag{A27}$$

The remaining problem to be solved is how to compute the complex function F_j.

Computational algorithms for F_j

Fast and accurate computational methods are required for the evaluation of F_j. For $|T| \ll 1$, the Maclaurin series expansion [34] is useful. For the other region except Re $T \ll -1$, we use the exact upward recursion relation

$$F_{j+1}(T) = \frac{(2j+1)F_j(T) - \exp(-T)}{2T}, \tag{A28}$$

and therefore all the F_j are obtained from F_0. Through a simple variable transformation, F_0 can be expressed by using the complementary error function (erfc)

$$F_0(T) = \frac{1}{2}\left(\frac{\pi}{T}\right)^{1/2}[1 - \mathrm{erfc}(T^{1/2})]. \tag{A29}$$

The function erfc is related to the Faddeeva function w by

$$\mathrm{erfc}(T^{1/2}) = \exp(-T)w(iT^{1/2}), \tag{A30}$$

and the computational algorithm for the Faddeeva function is available [35].

For Re $T \ll -1$, $|F_0|$ is too large to numerically calculate. In order to avoid the problem, we define

$$\tilde{F}_j(T) \equiv \exp(T)F_j(T), \tag{A31}$$

$$\tilde{R}_{N_xN_yN_z\,j}(T) \equiv \exp(T)R_{N_xN_yN_z\,j}(T). \tag{A32}$$

Then Eq. (A19) can be rewritten using $\tilde{R}_{N_xN_yN_z}$:

$$[N_xN_yN_z|r_C^{-1}] = \exp[-\alpha_P(\mathbf{P}-\mathbf{C})^2 + i\mathbf{PC}]\frac{2\pi}{\alpha_P}\tilde{R}_{N_xN_yN_z}(T). \tag{A33}$$

Multiplying both sides of Eqs. (A25a)–(A25c) by $\exp(T)$ yields the recursion relations for $\tilde{R}_{N_xN_yN_z\,j}$. The initial condition for $\tilde{R}_{N_xN_yN_z\,j}$ is given by $\tilde{R}_{000j}=(-2\alpha_P)^j\tilde{F}_j$, as in Eq. (A26). The counterparts of Eqs. (A28) and (A29) are

$$\tilde{F}_{j+1}(T) = \frac{(2j+1)\tilde{F}_j(T) - 1}{2T}, \tag{A34}$$

$$\tilde{F}_0(T) = \frac{1}{2}\left(\frac{\pi}{T}\right)^{1/2} \exp(T)[1 - \mathrm{erfc}(T^{1/2})], \qquad \text{(A35)}$$

respectively. For the case of $|T| \to \infty$ and $|\arg T^{1/2}| < 3\pi/4$, the asymptotic expansion of erfc is available [36]:

$$\mathrm{erfc}(T^{1/2}) \simeq \frac{\exp(-T)}{(\pi T)^{1/2}} \sum_{m=0}^{\infty} \frac{(-1)^m (2m-1)!!}{(2T)^m}, \qquad \text{(A36)}$$

where $(-1)!! \equiv 1$. This asymptotic expansion can be used in the case of $\mathrm{Re}\, T \ll -1$ which automatically satisfies $|\arg T^{1/2}| < 3\pi/4$. By inserting Eq. (A36) into Eq. (A35) and neglecting the first term in Eq. (A35) (since $|\exp(T)| \ll 1$), one obtains

$$\tilde{F}_0(T) \simeq -\sum_{m=0}^{\infty} \frac{(-1)^m (2m-1)!!}{(2T)^{m+1}}. \qquad \text{(A37)}$$

The larger $|T|$ is, the faster $\tilde{F}_0$ converges. Usually no more than several terms are required. From $\tilde{F}_0$, one can evaluate $\tilde{F}_j$ using Eq. (A34); then, $\tilde{R}_{N_x N_y N_z j}$ in Eq. (A33) are obtained.

[1] W. Heisenberg, Z. Phys. **120**, 513 (1943); C. Möller, K. Dan. Vidensk. Selsk. Mat. Fys. Medd. **23**, 1 (1945); G. F. Chew, Annu. Rev. Nucl. Sci. **9**, 29 (1959).

[2] L. V. Keldysh, Zh. Eksp. Teor. Fiz. **47**, 1945 (1964) [Sov. Phys. JETP **20**, 1307 (1965)].

[3] F. H. M. Faisal, J. Phys. B **6**, L89 (1973).

[4] H. R. Reiss, Phys. Rev. A **22**, 1786 (1980).

[5] F. H. M. Faisal and A. Becker, in *Selected Topics in Electron Physics*, edited by D. M. Campbell and H. Kleinpoppen (Plenum, New York, 1996); A. Becker and F. H. M. Faisal, Opt. Express **8**, 383 (2001).

[6] A. Becker and F. H. M. Faisal, J. Phys. B **38**, R1 (2005).

[7] See, e.g., (a) J. Muth-Böhm, A. Becker, and F. H. M. Faisal, Phys. Rev. Lett. **85**, 2280 (2000); (b) A. Becker and F. H. M. Faisal, *ibid.* **89**, 193003 (2002); (c) A. Jaron-Becker, A. Becker, and F. H. M. Faisal, Phys. Rev. A **69**, 023410 (2004).

[8] I. Kawata, H. Kono, and Y. Fujimura, J. Chem. Phys. **110**, 11152 (1999); I. Kawata and H. Kono, *ibid.* **111**, 9498 (1999).

[9] K. Harumiya, I. Kawata, H. Kono, and Y. Fujimura, J. Chem. Phys. **113**, 8953 (2000); K. Harumiya, H. Kono, Y. Fujimura, I. Kawata, and A. D. Bandrauk, Phys. Rev. A **66**, 043403 (2002).

[10] H. Kono, Y. Sato, Y. Fujimura, and I. Kawata, Laser Phys. **13**, 883 (2003).

[11] H. Kono, Y. Sato, N. Tanaka, T. Kato, K. Nakai, S. Koseki, and Y. Fujimura, Chem. Phys. **304**, 203 (2004).

[12] The existence of enhanced ionization is theoretically confirmed for one-electron and two-electron molecules such as H_2^+ and H_2. See, e.g., (a) S. Chelkowski, T. Zuo, and A. D. Bandrauk, Phys. Rev. A **46**, R5342 (1992); (b) T. Zuo and A. D. Bandrauk, *ibid.* **52**, R2511 (1995); (c) A. D. Bandrauk and H. Kono, in *Advances in Multi-Photon Processes and Spectroscopy*, edited by S. H. Lin, A. A. Villaeys, and Y. Fujimura (World Scientific, Singapore, 2003), Vol. 15, pp. 147–214; (d) T. Seidemann, M. Y. Ivanov, and P. B. Corkum, Phys. Rev. Lett. **75**, 2819 (1995); (e) M. Lein, T. Kreibich, E. K. U. Gross, and V. Engel, Phys. Rev. A **65**, 033403 (2002); (f) A. Saenz, *ibid.* **66**, 063407 (2002); (g) **66**, 063408 (2002); (h) L. Y. Peng, J. F. McCann, D. Dundas, K. T. Taylor, and I. D. Williams, J. Chem. Phys. **120**, 10046 (2004).

[13] K. Codling and L. J. Frasinski, J. Phys. B **26**, 783 (1993); J. H. Posthumus, A. J. Giles, M. R. Thompson, and K. Codling, *ibid.* **29**, 5811 (1996); E. Constant, H. Stapelfeldt, and P. B. Corkum, Phys. Rev. Lett. **76**, 4140 (1996); T. D. G. Walsh, F. A. Ilkov, S. L. Chin, F. Chateauneuf, T. T. Nguyen-Dang, S. Chelkowski, A. D. Bandrauk, and O. Atabek, Phys. Rev. A **58**, 3922 (1998); G. N. Gibson, M. Li, C. Guo, and J. P. Nibarger, *ibid.* **58**, 4723 (1998).

[14] A. Hishikawa, A. Iwamae, and K. Yamanouchi, Phys. Rev. Lett. **83**, 1127 (1999); S. Shimizu, J. Kou, S. Kawato, K. Shimizu, S. Sakabe, and N. Nakashima, Chem. Phys. Lett. **317**, 609 (2000).

[15] R. Itakura, K. Yamanouchi, T. Tanabe, T. Okamoto, and F. Kannari, J. Chem. Phys. **119**, 4179 (2003).

[16] R. Itakura, J. Watanabe, A. Hishikawa, and K. Yamanouchi, J. Chem. Phys. **114**, 5598 (2001); L. Robson *et al.*, Chem. Phys. Lett. **360**, 382 (2002); H. Harada *et al.*, J. Phys. Chem. A **107**, 6580 (2003).

[17] T. Helgaker and P. R. Taylor, in *Gaussian Basis Sets and Molecular Integrals*, edited by D. R. Yarkony (World Scientific, Singapore, 1995); I. R. Levine, *Quantum Chemistry* (Prentice-Hall, Englewood Cliffs, N.J., 2000).

[18] K. Mishima, K. Nagaya, M. Hayashi, and S. H. Lin, Phys. Rev. A **70**, 063414 (2004); J. Chem. Phys. **122**, 024104 (2005).

[19] A. Rudenko, K. Zrost, T. Ergler, A. B. Voitkiv, B. Najjari, V. L. B. de Jesus, B. Feuerstein, C. D. Schröter, R. Moshammer, and J. Ullrich, J. Phys. B **38**, L191 (2005).

[20] W. Becker, F. Grasbon, R. Kopold, D. B. Milošević, G. G. Paulus, and H. Walther, in *Atomic, Molecular, and Optical Physics*, edited by B. Bederson and H. Walther (Elsevier, New York, 2002), Vol. 48, p. 45.

[21] C. J. Joachain, *Quantum Collision Theory* (Noth Holland, Amsterdam, 1984).

[22] See, e.g., E. Cormier and P. Lambropoulos, J. Phys. B **29**, 1667 (1996).

[23] See, e.g., S. Ohara and A. Saika, J. Chem. Phys. **84**, 3963 (1985).

[24] M. W. Schmidt and K. Ruedenberg, J. Chem. Phys. **71**, 3951 (1979).

[25] See, e. g., Ref. 12(c); Z. Mulyukov, M. Pont, and R. Shakeshaft, Phys. Rev. A **54**, 4299 (1996).

[26] See, e.g., R. Dörner, Th. Weber, M. Weckenbrock, A. Staudte, M. Hattass, R. Moshammer, J. Ullrich, and H. Schmidt-Bocking, Adv. At., Mol., Opt. Phys. **48**, 1 (2002); A. Rudenko, K. Zrost, B. Feuerstein, V. L. B. de Jesus, C. D. Schröter, R. Moshammer, and J. Ullrich, Phys. Rev. Lett. **93**, 253001 (2004); A. Rudenko, K. Zrost, C. D. Schröter, V. L. B. de Jesus, B. Feuerstein, R. Moshammer, and J. Ullrich, J. Phys. B

37, L407 (2004).
[27] K. I. Dimitriou, D. G. Arbó, S. Yoshida, E. Persson, and J. Burgdörfer, Phys. Rev. A **70**, 061401(R) (2004).
[28] B. Delone and V. P. Krainov, J. Opt. Soc. Am. B **8**, 1207 (1991).
[29] P. B. Corkum, Phys. Rev. Lett. **71**, 1994 (1993).
[30] G. F. Bertsch, A. Schnell, and K. Yabana, J. Chem. Phys. **115**, 4051 (2001); M. A. L. Marques and E. K. U. Gross, Annu. Rev. Phys. Chem. **55**, 427 (2004); X. Chu and Shih-I Chu, Phys. Rev. A **70**, 061402(R) (2004).
[31] E. L. McMurchie and E. R. Davidson, J. Comput. Phys. **26**, 218 (1978).
[32] M. Tachikawa and M. Shiga, Phys. Rev. E **64**, 056706 (2001).
[33] S. F. Boys, Proc. R. Soc. London, Ser. A **200**, 542 (1950).
[34] F. E. Harris, Int. J. Quantum Chem. **23**, 1469 (1983).
[35] G. P. M. Poppe and C. M. J. Wijers, ACM Trans. Math. Softw. **16**, 47 (1990).
[36] *Handbook of Mathematical Functions*, 9th ed., edited by M. Abramowitz and I. A. Stegun (Dover, New York, 1970), p. 300.